

Kinematics of the CO Gas in the Inner Regions of the TW Hya Disk

Katherine A. Rosenfeld¹, Chunhua Qi¹, Sean M. Andrews¹, David J. Wilner¹, Stuartt A. Corder²,
C. P. Dullemond³, Shin-Yi Lin⁴, A. M. Hughes⁵, Paola D'Alessio⁶, and P. T. P. Ho⁷

ABSTRACT

We present a detailed analysis of the spatially and spectrally resolved ^{12}CO $J=2-1$ and $J=3-2$ emission lines from the TW Hya circumstellar disk, based on science verification data from the Atacama Large Millimeter/Submillimeter Array (ALMA). These lines exhibit substantial emission in their high-velocity wings (with projected velocities out to 2.1 km s^{-1} , corresponding to intrinsic orbital velocities $>20\text{ km s}^{-1}$) that trace molecular gas as close as 2 AU from the central star. However, we are not able to reproduce the intensity of these wings and the general spatio-kinematic pattern of the lines with simple models for the disk structure and kinematics. Using three-dimensional non-local thermodynamic equilibrium molecular excitation and radiative transfer calculations, we construct some alternative models that successfully account for these features by modifying either (1) the temperature structure of the inner disk (inside the dust-depleted disk cavity; $r < 4\text{ AU}$); (2) the intrinsic (Keplerian) disk velocity field; or (3) the distribution of disk inclination angles (a warp). The latter approach is particularly compelling because a representative warped disk model qualitatively reproduces the observed azimuthal modulation of optical light scattered off the disk surface. In any model scenario, the ALMA data clearly require a substantial molecular gas reservoir located inside the region where dust optical depths are known to be substantially diminished in the TW Hya disk, in agreement with previous studies based on infrared spectroscopy. The results from these updated model prescriptions are discussed in terms of their potential physical origins, which might include dynamical perturbations from a low-mass companion with an orbital separation of a few AU.

Subject headings: circumstellar matter — protoplanetary disks — planetary systems: formation — stars: individual (TW Hya)

¹Harvard-Smithsonian Center for Astrophysics, 60 Garden Street, Cambridge, MA 02138

²National Radio Astronomy Observatory, 520 Edgemont Road, Charlottesville, VA 22903

³Institut für Theoretische Astrophysik, Universität Heidelberg, Albert-Ueberle-Str. 2, 69120 Heidelberg, Germany

⁴Department of Physics, University of California San Diego, 9500 Gilman Drive, La Jolla, CA 92093

⁵University of California at Berkeley, Department of Astronomy, 601 Campbell Hall, Berkeley, CA 94720

⁶Centro de Radioastronomía y Astrofísica, Universidad Nacional Autónoma de México, Apartado Postal 72-3 (Xangari), 58089 Morelia, Michoacán, Mexico

⁷Academia Sinica Institute of Astronomy and Astrophysics, P.O. Box 23-141, Taipei 106, Taiwan

1. Introduction

In the standard model for star formation, the collapse of a slowly rotating molecular cloud core at least partially conserves its angular momentum by forming a compact, flattened disk that channels mass onto a central protostar (Cassen & Moosman 1981; Terebey et al. 1984). Once the remnant core material is accreted or dispersed, the gravitational potential of the star determines the kinematic properties of its disk. At that time, the intrinsic disk velocity field should be described well by a Keplerian pattern of differential rotation in circular orbits, $v_\phi(r) = v_k = \sqrt{GM/r}$, where ϕ is the azimuthal direction in a polar coordinate system, G is the gravitational constant, r is the distance from the star, and M is the mass enclosed within r . In most cases, the disk-to-star mass ratio is low enough that $M \approx M_\star$ is a reasonable approximation. Imaging spectroscopy data taken with millimeter interferometers first verified these signatures of disk rotation using the optically thick emission lines of the carbon monoxide (CO) molecule (Koerner et al. 1993; Dutrey et al. 1994; Koerner & Sargent 1995; Mannings & Sargent 1997). Subsequent work demonstrated that the rotation patterns were indeed Keplerian ($v_\phi \propto r^{-0.5}$) and could be used to make dynamical estimates of central star masses (Guilloteau & Dutrey 1998; Dutrey et al. 1998; Simon et al. 2000).

In practice, spectral imaging observations measure the intrinsic velocity field projected onto the sky, $v_{\text{obs}} = v_\phi \sin i$, where i is the angle between the disk rotation axis and the observed line of sight (e.g., $i = 0^\circ$ corresponds to face-on). A Keplerian velocity field can be exploited to probe gas at small radii in the disk, even if the angular resolution of the observations is relatively limited (e.g., Dutrey et al. 2008). This kind of physically motivated super-resolution can be achieved with a focus on the intensities (and ideally morphologies) in the high-velocity wings of emission lines. For optically thick lines like those produced by the rotational transitions of CO, the line strength depends on the product of the gas temperature and emitting area (e.g., Beckwith & Sargent 1993). Since the projected emitting areas are typically small in the inner disk, emission in the line wings is generally weak; often well below the sensitivity thresholds for most millimeter-wave interferometers.

To further complicate issues, there are theoretical mechanisms and disk properties that could modify this simple prescription for interpreting the projected disk velocity field. For example, in a very massive disk, gravitational instabilities could excite spiral waves that drive significant (radial) streaming motions. This was suggested as a potential explanation for the complex kinematic environment of the AB Aur disk (Lin et al. 2006), although others have associated its (possibly) non-Keplerian motions with envelope contamination (Piétu et al. 2005; Corder et al. 2005). Gas pressure gradients also lead to deviations from Keplerian orbits: the sub-Keplerian shift expected from thermal (hydrostatic) pressure is too small to observe directly (Weidenschilling 1977), but magnetic pressure might have a more substantial influence over gas motions (e.g., Shu et al. 2007, 2008). Alternatively, a disk might *appear* to have non-Keplerian motions (even if $v_\phi = v_k$ exactly) if its line-of-sight orientation (i) varies with radius – that is, if the disk structure is warped.

Given that emission line wings are typically expected to be weak, disentangling these subtle (hypothetical) modifications to a simple projected velocity field from the intrinsic properties of the

inner disk makes for a difficult task in data analysis. Nevertheless, the potential for this unique access to the spatio-kinematic properties and physical conditions of the gas in the innermost regions of protoplanetary disks is extraordinarily compelling. Perhaps the best opportunity to explore these features is with the massive, gas-rich disk around the nearest ($d \approx 54$ pc; van Leeuwen 2007) classical T Tauri star, TW Hya. Aside from the enhanced sensitivity and spatial resolution afforded by its proximity, the TW Hya disk coincidentally has the added benefits of a nearly face-on viewing geometry ($i \approx 6\text{--}7^\circ$; Krist et al. 2000; Qi et al. 2004; Hughes et al. 2011). This means that the line wing emission generated by gas in the inner regions of the TW Hya disk has relatively small observed Doppler shifts from the systemic velocity. Because the low disk inclination angle minimizes radial projection effects, subtle departures from a simple (unwarped, Keplerian) model for the projected velocity field should be more easily recognizable observationally.

In this article, we take advantage of the dramatically improved sensitivity now available in the Science Verification (SV) data products from the Atacama Large Millimeter/Submillimeter Array (ALMA) to help characterize the spatio-kinematic morphologies of the spatially and spectrally resolved CO $J=2-1$ and $J=3-2$ emission lines from the TW Hya circumstellar disk. A brief overview of the data and its calibration are presented in §2. The data is investigated in detail in §3, using emission line radiative transfer calculations and considering various toy models for the disk properties. The results are synthesized in the larger context of the structure and kinematics in the inner regions of the TW Hya disk in §4, and summarized in §5.

2. Data and Calibration

The TW Hya disk was observed with nine 12-m elements of ALMA as part of the commissioning and SV effort during construction. These data were obtained in two (contiguous) ~ 4.5 -hour observations, using receiver bands 6 and 7 on 2011 April 20 and 22, respectively, with antenna spacings providing baseline lengths of $\sim 20\text{--}100$ m (one antenna was not available for band 7 observations at this time). The ALMA correlator was configured to simultaneously observe four 0.5 GHz-wide spectral windows (two in each sideband) with a 122 kHz channel spacing in each window. One of those windows was centered near the $^{12}\text{CO } J=2-1$ line (230.538 GHz) in band 6 and the $^{12}\text{CO } J=3-2$ line (345.796 GHz) in band 7, providing a velocity spacing of 0.16 and 0.11 km s $^{-1}$, respectively. The ALMA correlator Hanning smoothes the data, making the effective spectral resolution coarser (~ 0.3 and 0.2 km s $^{-1}$ in bands 6 and 7). Two other spectral windows were designed to provide ~ 1 GHz of continuum bandwidth in each receiver band; the remaining windows contained weaker spectral lines that are not of interest here. Observations cycled between TW Hya and the nearby complex gain calibrator J1037-295 every ~ 10 minutes. The bright quasar 3C 279 was observed as a bandpass calibrator, and brief observations were made of Titan for absolute flux calibration.

These data were calibrated in the CASA software package (v3.3), carefully following the detailed processing scripts kindly provided by the ALMA science verification team. Since those instructions,

along with fully calibrated measurement sets, are publicly available online¹, we do not repeat the details here. The continuum-subtracted, calibrated spectral visibilities for each CO emission line were Fourier inverted (assuming natural weighting) with modest spectral averaging, deconvolved with the CLEAN algorithm using a simple polygon mask applied to all channels, and restored with a synthesized beam of dimensions $2''.8 \times 2''.4$ (at a P.A. of 44°) for $J=2-1$ and $1''.7 \times 1''.5$ (P.A. = 22°) for $J=3-2$. We utilized two different channel spacings: (1) “native”, meaning 0.20 and 0.12 km s^{-1} for $J=2-1$ and $J=3-2$, respectively, to highlight the key kinematic features (note that this over-samples the true spectral resolution; this is the averaging advocated in the ALMA calibration tutorials), and (2) “binned”, meaning 0.35 km s^{-1} for both lines, to simplify comparisons and sample models closer to the true Hanning-smoothed velocity resolution. The resulting spectral image cubes are indistinguishable from the reference datasets provided by the science verification team, with one small distinction: we elected to force the reduced spectral datasets to have a channel precisely centered on the known systemic LSR velocity of TW Hya, $+2.87 \text{ km s}^{-1}$.

The CO $J=2-1$ and $J=3-2$ line emission from the TW Hya disk are shown as channel maps in Figures 1 and 2, respectively, with a logarithmic color-scale stretch to emphasize emission over a wide dynamic range (a scale bar is marked on the top of each figure). Measurements of the RMS noise levels, peak and integrated line intensities for each transition are compiled in Table 1. The channel maps clearly show a resolved pattern of rotation, from the blueshifted northwest to the redshifted southeast (with a major axis position angle of 151°), around the systemic velocity and centered at the stellar position (Qi et al. 2004, 2006). While these are not the highest spectral (see Hughes et al. 2011) or spatial (see Andrews et al. 2012) resolution views of CO emission from the TW Hya disk, they are by far the most sensitive ($\sim 10\times$ higher S/N). This enhanced sensitivity reveals a surprising spectral feature: significant ($>5\sigma$) emission in the wings of both CO transitions out to projected velocities at least $\pm 2.1 \text{ km s}^{-1}$ from the line centers.

We will demonstrate in §3 that these line wings are primarily generated well inside a radius of $\sim 5 \text{ AU}$ in the TW Hya disk and, coupled with the emission morphology near the systemic velocity, they are difficult to reproduce for a disk in Keplerian rotation with a nearly face-on viewing geometry and smoothly-varying temperature profile. Because of the value of this *relatively* faint emission at high velocities in what follows, we conducted a variety of tests to ensure that these line wings were not artificially generated in the calibration process. First, we verified that the disk emission is not spectrally coincident with CO features in the Earth’s atmosphere. Weak and narrow CO absorption ($\sim 1 \text{ MHz}$ wide; $\sim 10\text{-}20\%$ depths) was noted and flagged in the observations of the bandpass calibrator 3C 279: however, they are located $\gtrsim 20 \text{ MHz}$ from the TW Hya line center, and are therefore well outside the spectral range of interest here. A second test focused on the remote possibility that the application of the frequency-dependent system temperatures (T_{sys}) could have artificially broadened the lines. In these data, a coarse measure of the spectral T_{sys} behavior was determined directly from observations of TW Hya. The concern is that the bright CO emission

¹<https://almascience.nrao.edu/alma-data/science-verification>.

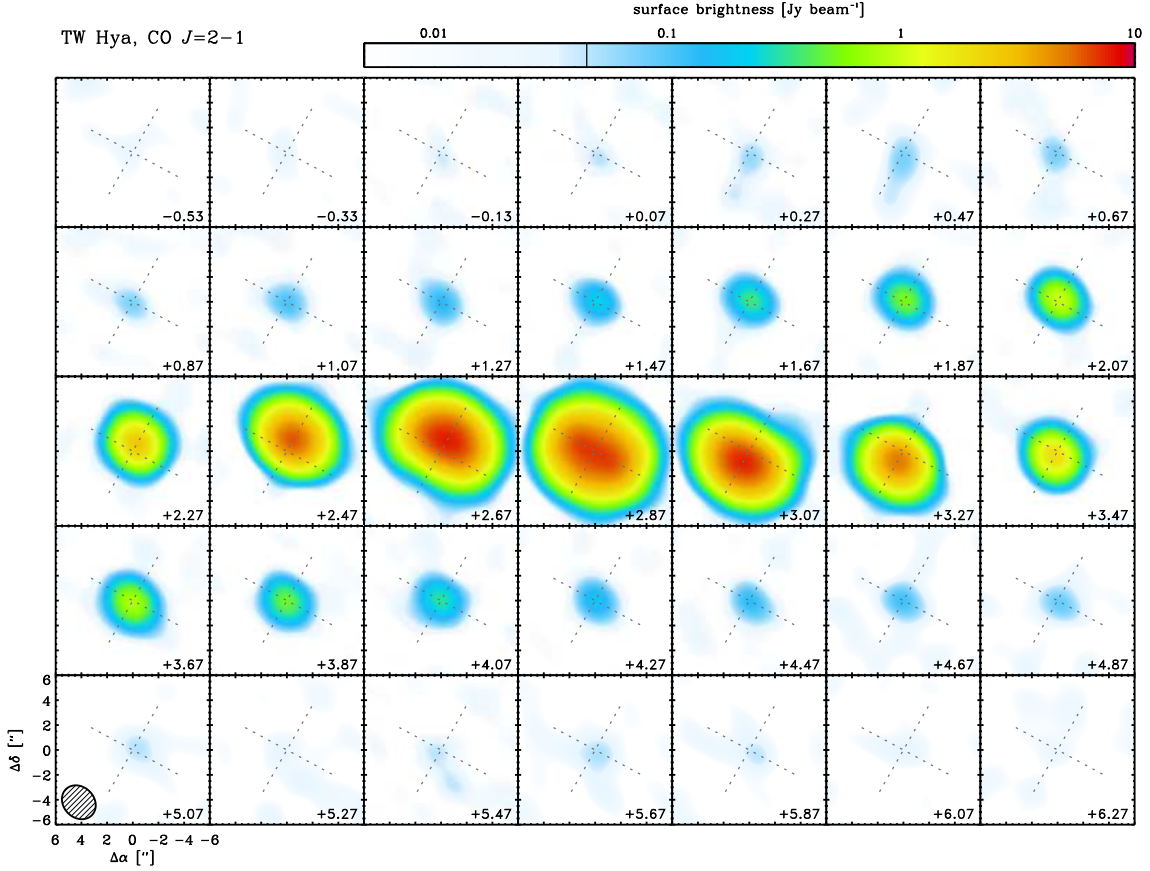


Fig. 1.— Channel maps of the CO $J=2-1$ line emission from the TW Hya disk, with a “native” velocity-spacing of 0.20 km s^{-1} . A logarithmic color-scale bar (*top*) indicates the line intensities, with a vertical line representing the 5σ level (see Table 1). Each panel is $12''$ on a side, corresponding to a projected physical scale of $\sim 650 \text{ AU}$. Cross-hatches mark the stellar position and orientation of the disk major axis (151° east of north). The synthesized beam dimensions are drawn in the bottom left panel; LSR velocities (in km s^{-1}) are marked in the bottom right of each panel.

from the disk might produce a weak, but broad feature in the T_{sys} profile that would then be propagated into the data as faint emission wings. To test this, we re-calibrated the data instead with a spectrally flat, band-averaged T_{sys} correction. This had no discernable effect on the results; the observed line wings persist at the same intensity levels. Finally, we investigated whether the continuum subtraction process could be responsible. A wide range of techniques were attempted, varying the polynomial order and channel ranges employed to determine the underlying continuum level on either side of the emission line. In all cases, we found no significant difference in the resulting line wings (indeed, they are even present without any continuum subtraction applied). To summarize, we find no obvious artificial mechanism in the data acquisition or calibration procedures that can produce these substantial emission line wings with the same velocity-widths in two CO

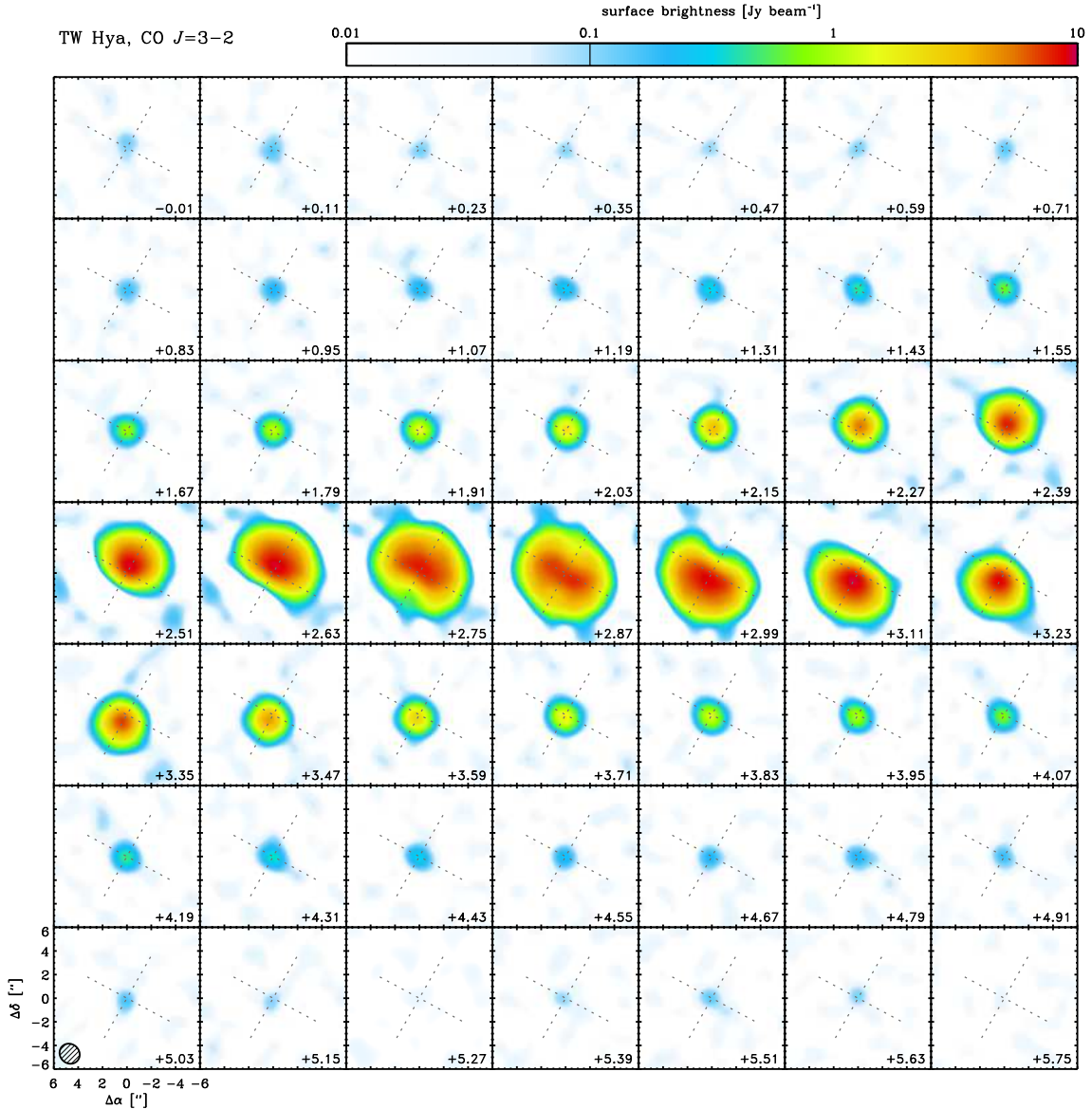


Fig. 2.— Same as Figure 1, but for the CO $J=3-2$ line.

transitions observed at different times and with different receivers and spectral setups.

3. Analysis

Having presented the ALMA data (see Figures 1 and 2), we now turn to its interpretation with a special emphasis on the resolved spatio-kinematic patterns of the CO emission lines. First, we briefly describe a generic framework for producing models of the CO lines in the TW Hya disk

(§3.1). Next, we demonstrate that standard models are unable to reproduce the ALMA data with the typical assumptions about disk temperature profiles and the spatial variation of the disk velocity field projected on the sky (§3.2). Then, we present three options for simple modifications to those assumptions that are able to reconcile the data and models (§3.3): a large temperature increase inside the TW Hya disk cavity ($r \leq 4$ AU; §3.3.1); a deviation from a Keplerian velocity field that produces relatively enhanced rotation rates at small disk radii (§3.3.2); or a warp that produces a relatively higher line-of-sight inclination angle in the inner disk (§3.3.3). We focus on a qualitative illustration of how the data reveal novel spatio-kinematic information on gas at small radii in the TW Hya disk, rather than employing a quantitative model-optimization (detailed fitting) approach: the latter will be more useful in the near future, when ALMA provides TW Hya data with further improvements in dynamic range and angular resolution (as well as sensitivity).

3.1. Modeling Overview

We defined a simple, azimuthal- and mirror-symmetric parameterized model for the disk gas densities on a cylindrical grid with coordinates (r, ϕ, z) , such that

$$\rho(r, z) = \frac{\Sigma}{\sqrt{2\pi}H_p} \exp\left[-\frac{1}{2}\left(\frac{z}{H_p}\right)^2\right], \quad (1)$$

where Σ and H_p are the radial surface density and pressure scale height profiles, respectively. For the former, we adopted the similarity solution for a simple viscous accretion disk (Lynden-Bell & Pringle 1974; Hartmann et al. 1998, see also Andrews et al. 2009, 2010),

$$\Sigma(r) = \Sigma_c \left(\frac{r}{r_c}\right)^{-\gamma} \exp\left[-\left(\frac{r}{r_c}\right)^{2-\gamma}\right], \quad (2)$$

where γ is the gradient parameter that describes the power-law radial variation of the disk viscosity, r_c is a characteristic scaling radius, and $\Sigma_c = e \cdot \Sigma(r_c)$. Since we considered only emission from the CO molecule, the models were parametrically defined in terms of the CO column density,

$$N_{\text{co}}(r) = \frac{X_{\text{co}}}{\mu m_H} \Sigma(r), \quad (3)$$

where X_{co} is the CO abundance fraction in the gas, $\mu = 2.37$ is the mean molecular weight of the gas, and m_H is the mass of a hydrogen atom. The scale height profile was set by the balance of gravity and thermal pressure in the disk, such that

$$H_p(r) = \frac{c_s}{\Omega} = \left[\frac{k_b r^3 T(r)}{GM_* \mu m_H}\right]^{1/2}, \quad (4)$$

where c_s is the local sound speed, Ω is the Keplerian angular velocity, and k_b is the Boltzmann constant. In this formulation, we implicitly assumed that the disk is vertically isothermal (at each

radius), with a radial temperature profile $T(r) = T_{10}(r/10 \text{ AU})^{-q}$, where $T_{10} = T(10 \text{ AU})$. The disk kinematics are determined by a velocity field in the model plane, $\vec{v} = (v_r, v_\phi, v_z)$. In the models considered here, $v_r = v_z = 0$, and the azimuthal component of \vec{v} is described by Keplerian rotation,

$$v_\phi(r) = v_k = \sqrt{\frac{GM_*}{r}}, \quad (5)$$

assuming implicitly that the disk mass is negligible compared to the stellar mass.

The structure model described in Equations (1)-(5) is fully characterized by a set of 6 parameters, $\{N_c, r_c, \gamma, T_{10}, q, M_*\}$.² An additional 3 parameters are required to convert this structure to a synthetic CO emission line model projected into the sky plane: a turbulent velocity dispersion (ξ), and a disk viewing geometry specified by the inclination (i) and major axis position angle (PA). For a given set of 9 parameters, we used the three-dimensional non-local thermodynamic equilibrium (non-LTE) molecular excitation and radiative transfer code LIME (v1.02; Brinch & Hogerheijde 2010) and the data from the LAMBDA database (Schöier et al. 2005) to calculate level populations and generate high-resolution synthetic spectral cubes for the CO $J=2-1$ and $J=3-2$ emission lines. Those cubes were Fourier transformed and re-sampled onto the spectral and spatial frequency grids employed in the ALMA observations. The resulting model spectral visibilities were then passed through the same CASA imaging processes that were performed on the data (see §2).

3.2. The Failure of Standard Models

We first constructed a “fiducial” model using the standard parameterization described in §3.1, motivated by the results of our previous analyses of CO emission from the TW Hya disk (Qi et al. 2004, 2006; Hughes et al. 2008, 2011; Andrews et al. 2012). Because of the time-consuming nature of the LIME calculations for any given model, we adopted a simplistic exploration of parameter-space that utilized the modified Levenberg-Marquardt minimization algorithm MPFIT (Markwardt 2009) to help find parameters that produced a low χ^2 in the spectral visibilities for both CO transitions. In that process, we forced the basic parameters that describe the disk densities $\{N_c, \gamma, r_c\}$ and turbulent velocity width $\{\xi\}$ to be the same for both CO transitions, but allowed different values for the temperature profile parameters $\{T_{10}, q\}$ for the two emission lines. The fiducial stellar mass was fixed to $M_* = 0.8 M_\odot$ (e.g., Wichmann et al. 1998; Hughes et al. 2011), and the major axis position angle was set to 151° (east of north); the disk inclination $\{i\}$ was considered a free parameter (albeit the same for both CO transitions). Guided by the minimization results, the model parameters were slightly adjusted manually to best reproduce the observed channel maps (at native resolution). The fiducial model parameters we derived are provided in Table 2 (not surprisingly, they are similar to those for the Model sA constructed by Andrews et al. 2012). The model channel maps are compared directly with the data in Figure 3, imaged on the binned velocity grid with the same channel-spacing of 0.35 km s^{-1} for both CO transitions, for clarity.

² N_c is defined as the CO column density at the characteristic radius, r_c ; see Equation (3).

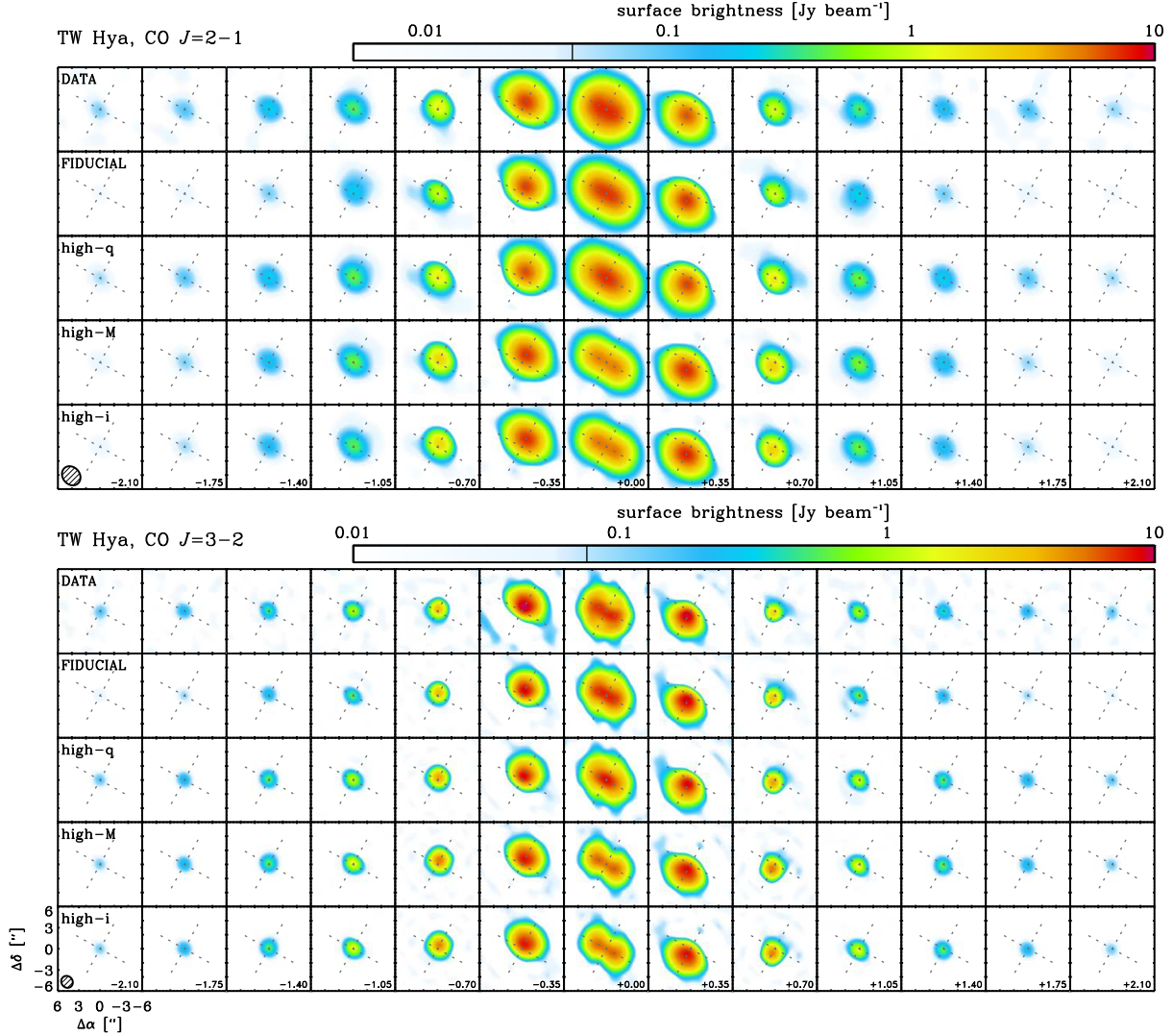


Fig. 3.— Comparisons of the observed CO $J=2-1$ and $J=3-2$ channel maps (*top rows*) with the fiducial model and the three other standard models described in §3.2 (see Table 2 for parameter values). The observed and model channel maps were synthesized on the same binned 0.35 km s^{-1} velocity gridding for ease of comparison. The map sizes, intensity scale bars, LSR velocity labels, and synthesized beam dimensions are the same as in Figures 1 and 2.

The fiducial model is a good match to the ALMA data near the systemic velocity, but notably fails to reproduce the emission line wings that are observed for both CO transitions. Those wings are observed at velocities at 2.1 km s^{-1} (and beyond, albeit at lower statistical significance) from the line core, corresponding to intrinsic disk velocities in excess of 20 km s^{-1} considering the inferred disk inclination of $\sim 6^\circ$. For this stellar mass and assuming Keplerian orbits, those velocities are only reached at disk radii $< 2 \text{ AU}$. Since these CO lines have such high optical depths, their intensities

scale with the product of the gas temperature and the projected emitting area (Beckwith & Sargent 1993; Dutrey et al. 1994). With such a small area available to produce emission at these line wing velocities, this discrepancy between the fiducial model and the data is perhaps not so surprising. Broadly speaking, there are two approaches that could help reproduce the observed CO emission line wings: the first deals with adjusting the physical conditions of the model at small radii, and the second relies on modifying the model parameters that control the projected velocity field.

For the first (structure) approach, a representative model needs to incorporate higher gas temperatures at small disk radii (because the optical depth is so high, adjustments to the CO column densities have little effect on the line wing emission strengths). Sticking with the standard prescription for modeling this kind of data (described in §3.1), that requirement effectively amounts to adopting a steeper temperature profile. We constructed such a “high- q ” model with a larger radial temperature gradient ($q = 0.65$); parameter values are listed in Table 2, and synthetic channel maps are compared directly with the data and fiducial model in Figure 3. By increasing the gas temperatures inside ~ 5 AU by roughly a factor of 3, this kind of model is able to reproduce the observed intensities in the emission line wings. However, the required temperature profile is too steep to properly account for the emission morphology generated at relatively large disk radii, and therefore ends up being a very poor match for the CO emission near the systemic velocity.

The alternative (kinematic) approach relies on increasing the projected area of the high-velocity disk region responsible for producing the CO line wings. Put simply, the observations demand an increase in the projected velocity field ($v_{\text{obs}} = v_{\phi} \sin i$). This can be achieved either by scaling up the intrinsic disk velocities ($v_{\phi} = v_k \propto \sqrt{M_*}$) and/or the projected line of sight ($\sin i$). To demonstrate that, we constructed two additional models using the standard prescription outlined in §3.1. First, a “high- M_* ” model employed a larger stellar mass ($M_* = 1.5 M_{\odot}$) to speed up the Keplerian orbital velocities (v_{ϕ}), thereby increasing the extent of the high-velocity emitting area. And second, a similar effect was achieved for a “high- i ” model that adopts a more inclined viewing geometry ($i = 8^{\circ}$). Both of these models increase the projected line of sight velocities by a factor of ~ 1.4 , which corresponds to a factor of ~ 3.5 -4 increase in the emitting area that produces the high-velocity line wings. The parameters for these models are listed in Table 2. Their corresponding synthetic channel maps are compared with the data and fiducial model in Figure 3. As expected, the high- M_* and high- i models successfully reproduce the observed CO line wings: however, they consequently do a very poor job accounting for the morphology near the systemic velocity.

In practice, the high- q , high- M_* , and high- i models that follow the standard formalism outlined in §3.1 all fail to reproduce the observed CO emission line morphologies *in the same way*.³ No reasonable combinations of q , M_* , and i can simultaneously reproduce both the CO line wings and the emission morphology near the systemic velocity. Uniformly scaling up the temperature profile

³From a statistical perspective, these kinds of model are formally much poorer matches to the data than the fiducial model: their discrepancies with the data are primarily in the spectral channels that contain most of the emission signal, and therefore most of the weight (contribution to χ^2) in any quantitative assessment of fit quality.

gradient or projected velocity field at all disk radii cannot explain the patterns of the ALMA data.

3.3. Alternative Models

The standard modeling formalism explored in §3.2 is unable to explain the observed spatio-kinematic emission morphologies of the CO emission lines generated by the TW Hya disk. However, that modeling effort demonstrated clearly the “sense” of this failure. To produce the emission line wings, we need a model with either much higher temperatures or increased projected velocities in the inner disk. However, the observed emission morphology near the systemic velocity was explained best with a fiducial temperature structure and projected velocity field. This implies that we require a deviation from the standard structure and kinematics model that *varies with radius* in the disk. As before, these modifications to $T(r)$ or $v_{\text{obs}}(r) = v_{\phi} \sin i$ can be manifested in a deviation to the form of the temperature profile, the intrinsic disk velocity field, $v_{\phi}(r)$, and/or the disk viewing angle, $i(r)$, so long as those functional forms *decrease* with r . Three such alternatives were explored here, using simple parametric adjustments to the standard model prescription.

3.3.1. A Hot Inner Disk

The first approach we adopted for these alternative models was to implement a structural modification to the radial temperature profile. As was shown in §3.2, models with a hot inner disk (steeper gradient q) are able to reproduce the observed CO line wing intensities, but the outer disk needs to have a more shallow temperature profile to account for the emission morphology near the line core. In principle, these features could be reconciled by permitting the gradient parameter q to vary with radius. However, such a modification is not so intuitive; instead, we elected to simply permit a multiplicative scaling of the temperatures inside a given radius, such that

$$T(r) = (\delta T) \cdot T_{10} (r/10\text{AU})^{-q} \quad (6)$$

where δT is a free (constant) parameter in the inner disk, but $\delta T = 1$ when $r > r_{\text{hot}}$. In effect, this model adjustment preserves the fiducial outer disk temperature profile, but artificially scales up the temperatures at small disk radii to produce the CO line wings. Based on this modified framework, we developed a representative model for the CO emission following the procedure described in §3.2. The resulting parameters for this “hot” model are listed in Table 2. Synthetic observations of the model are compared with the data as channel maps in Figure 4, as well as in position-velocity diagrams (constructed from a slice along the disk major axis) in Figure 5.

We find a good match to the CO data by modifying the fiducial model described in §3.2 with a scaling factor $\delta T = 3$ inside a radius $r_{\text{hot}} = 4 \text{ AU}$. This choice for r_{hot} was not arbitrary; it was selected because the TW Hya disk is known to have substantially diminished dust optical depths inside that radius (Calvet et al. 2002; Hughes et al. 2007; Arnold et al. 2012). Notably, the implicit assumption for this scenario is that a substantial gas reservoir is still present inside the dust cavity.

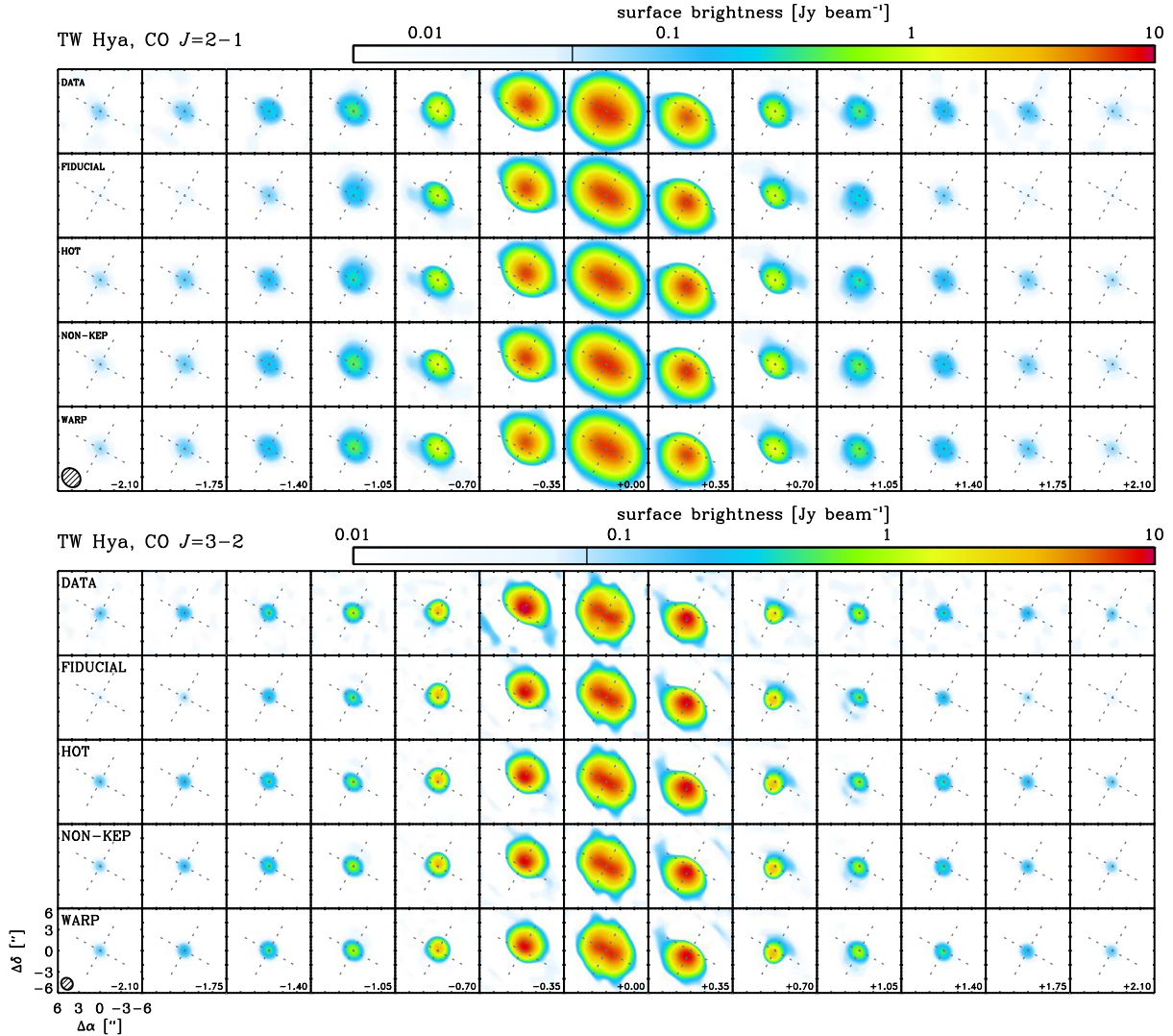


Fig. 4.— A channel map comparison of the data, fiducial model, and the alternative models described in §3.3 (similar to Figure 3). Model parameters are listed in Table 2.

3.3.2. A Non-Keplerian Velocity Field

The second alternative we considered was a kinematic modification to the intrinsic velocity field of the gas in the inner disk. Again, as demonstrated in §3.2, the outer disk velocities can not also be scaled up without producing large deviations in the observed emission morphology near the systemic velocity. To accomodate both requirements, we introduced a simple scaling factor for the disk velocity field, $v_\phi(r) = f v_k$ (see Equation 5). The scaling factor f describes the model deviation

from Keplerian orbits and is permitted to vary with radius like a power-law in the inner disk,

$$f(r) = \begin{cases} (r/r_b)^{-x} & \text{if } r \leq r_b \\ 1 & \text{if } r > r_b \end{cases} \quad (7)$$

where $\{r_b, x\}$ are free parameters that describe a break radius and the gradient of the scaling function, respectively. In the standard models described in §3.1 and 3.2, $f = 1$ at all disk radii (effectively, $x = 0$ in those cases). Adding in this parametric non-Keplerian scaling factor as a slight modification to the standard modeling framework, we constructed representative models for the CO emission lines using the procedure outlined above. The resulting parameter values are listed in Table 2; the model is compared with the ALMA data in Figures 4 and 5.

Adopting $r_b \approx 60$ AU and $x = 0.15$ to describe f , we were able to reproduce well the observed CO line wings without sacrificing the fit quality of the emission morphology near the systemic velocity. The super-Keplerian rotation in the inner disk means that the CO emitting area at the observed velocities of the line wings is substantially enhanced relative to the fiducial model (by a factor of ~ 5), and therefore able to generate high-velocity emission at roughly the observed levels. The $\{r_b, x\}$ values adopted here are not unique (nor optimized); a smaller break radius and larger gradient (or vice versa) could probably accommodate the data with a similar fit quality. However, these values and this *kind* of model modification are sufficient to demonstrate the key point: a non-Keplerian deviation in the disk velocity field which decreases with radius successfully accounts for the observed spatio-kinematic CO structure emitted by the TW Hya disk.

3.3.3. A Disk Warp

We explored another kinematic alternative model that incorporates a warp in the vertical structure of the gas disk. Rather than raise the intrinsic orbital velocity of the gas (v_ϕ), this model increases the observed velocity by changing the line of sight ($\sin i$) as a function of radius. In this way, a warp – or a disk inclination that *increases* toward the central star – raises the projected velocities in the inner disk, effectively increasing the emitting area at a given observed velocity. If the inclination is a decreasing function of r , this model can be designed to have minimal impact on the kinematic pattern for the outer disk, promoting a favorable emission morphology near the systemic velocity. To construct a warped disk model, we introduced a power-law profile for the observed inclination angles,

$$i(r) = i_0 \left(\frac{r}{r_0} \right)^{-y}, \quad (8)$$

aligned with the disk major axis (assuming a vertically thin disk; see the Appendix), where $\{i_0, y\}$ are parameters that describe the inclination normalization (at r_0) and its radial gradient, respectively. For a given set of structure parameters, the model densities and temperatures are rotated to this modified viewing geometry. The velocity field is tilted using a quaternion transformation, as described in more detail in the Appendix. Incorporating this parametric formulation for a warped

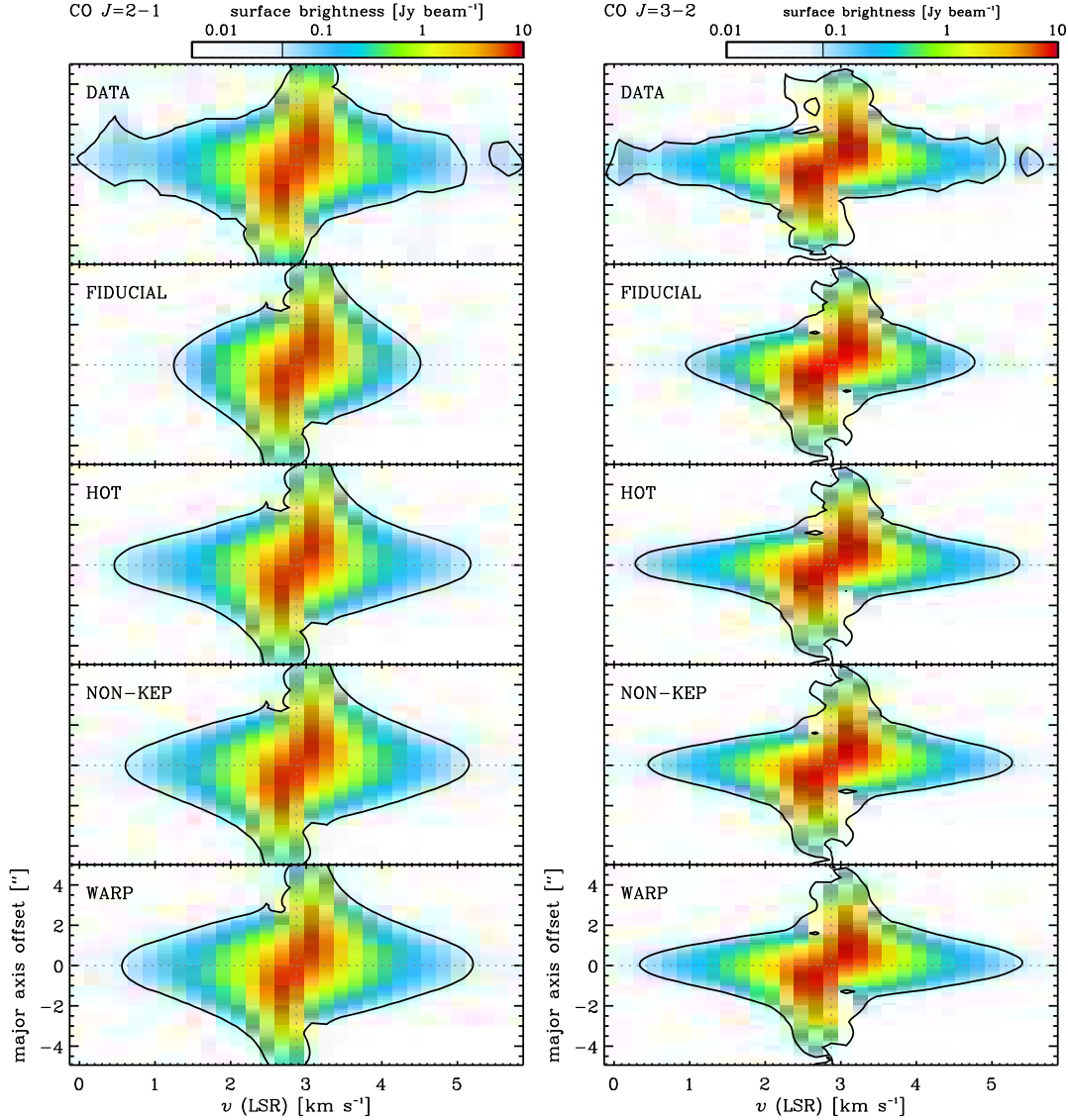


Fig. 5.— CO position-velocity diagrams constructed from a cut along the disk major axis (P.A. = 151°) for the data and the fiducial, hot, non-Keplerian, and warped models described in §3.3. For reference to gauge the extent of the line wings, the 5σ brightness level is marked with a contour.

disk viewing geometry, we constructed models for the TW Hya CO emission lines as before. The resulting parameter values for a representative warped model are included in Table 2; synthetic observations of the models are compared with the data in Figures 4 and 5.

Models that include a modest warp, with $i_0 \approx 8^\circ$ at $r_0 = 5$ AU and a gradient $y = 0.15$, provide an excellent match with the ALMA data for both CO emission lines, reproducing well the observed line wings and emission morphology near the systemic velocity. Like the non-Keplerian

model described in §3.3.2, this warp formulation successfully produces high-velocity line emission by increasing the projected CO emitting area at the observed wing velocities by a factor of ~ 5 (by design). And also like that case, the warp model parameters we determine or even the formulation we adopt are not unique, nor optimized. Instead, they are intended to conceptually verify that a warped disk geometry can reproduce in detail the fundamental features of the observed CO line emission with the addition of only a single model parameter; an inclination gradient, y .

3.4. Additional Comments

It is worth pointing out that the alternatives discussed in the previous subsections are in no way mutually exclusive: various combinations of these effects could be used to achieve similar results. Moreover, there are additional alternatives to a simple disk model that could presumably account for these ALMA observations, but have not been explored in detail here. Perhaps most compelling among these is a model that explicitly incorporates a spatial variation in the broadening term of the line profile. For example, it seems reasonable that a model with a turbulent line width ξ that decreases with radius should be able to re-distribute some emission into the high-velocity line wings observed here. The ξ values we adopted are commensurate with the turbulence constraints imposed by Hughes et al. (2011) for the outer disk, made using observations with $\sim 4\text{--}5\times$ higher spectral resolution than the ALMA data. However, we cannot rule out higher ξ values at small disk radii. We attempted a simple modification to our fiducial model that permits the turbulent velocity widths to scale with the sound speed of the gas, using the Hughes et al. (2011) upper limit to normalize $\xi(r)$ in the outer disk: but given the low ξ at large r and modest radial variation of c_s , this has little effect on the CO line wings. If a variable turbulent line width parameter is the origin of these wings, ξ must increase more steeply than c_s in the inner disk. Given the limited velocity resolution of these ALMA data relative to the subsonic turbulent velocity dispersions in the TW Hya disk, we felt it was premature to push the further exploration of such models. Nevertheless, it remains an interesting possibility that could be investigated with future observations.

4. Discussion

We have conducted a detailed analysis of the $^{12}\text{CO } J=2-1$ and $J=3-2$ line emission from the gas-rich disk around the nearby young star TW Hya, making extensive use of the science verification data from the Atacama Large Millimeter Array (ALMA) commissioning effort. With the substantial improvement in line sensitivity afforded by ALMA (even during its construction), we identified a novel feature in these CO spectra: the presence of relatively faint line wing emission extending out to high projected velocities of at least $\pm 2.1 \text{ km s}^{-1}$ from the (systemic) line center, roughly twice the maximum velocities previously inferred for the TW Hya disk from less sensitive data (Qi et al. 2004, 2006; Hughes et al. 2011; Andrews et al. 2012). Given the nearly face-on viewing geometry of the TW Hya disk, gas on Keplerian orbits that generates these line wings must be located within

a few AU from the central star. This kinematic super-resolution was employed in an exploration of the temperature and velocity structure of the inner disk, utilizing a non-local thermodynamic equilibrium molecular excitation and radiative transfer code and a standard modeling prescription for circumstellar disks. We found that the typical assumptions of a simple, Keplerian disk with a smooth gas temperature profile were unable to simultaneously produce both the CO line wings and the observed line emission morphology near the systemic velocity. Instead, we developed three alternative model possibilities that are able to qualitatively account for the ALMA data by making small (parametric) adjustments to the spatio-kinematic structure of the gas in the inner disk.

In one such alternative, we considered a parametric scaling of the gas temperatures inside the known dust-depleted cavity at the disk center ($r < 4$ AU; Calvet et al. 2002; Hughes et al. 2007) in an effort to boost the CO line wing intensities without substantially disturbing the emission morphology near the line core. With the outer disk structure based on a fiducial model, an increase of the gas temperatures in the dust cavity by a factor of ~ 3 successfully accounts for the ALMA CO observations. While such a temperature scaling might seem simplistic and artificial, it is in fact consistent with continuum radiative transfer models for the TW Hya disk: the low optical depths inside the disk cavity mean that stellar radiation is effectively unattenuated, leading to substantial heating (Calvet et al. 2002; Andrews et al. 2012). If we assume that gas and dust temperatures are correlated (if not identical), then the factor $\delta T \approx 3$ derived here is quite reasonable. For reference, the models developed by Andrews et al. (2012) have dust temperatures that increase by a factor of ~ 4 over a narrow (~ 1 AU-wide) region around the cavity radius (see their Figure 3). It is interesting to consider the key implication of this model: the CO emission line wings detected by ALMA may offer an indirect (and not very practical) observational signature of a low-density dust cavity, but they also *require* that this cavity still hosts a significant reservoir of molecular gas.

Of course, the presence of gas inside the TW Hya disk cavity has been inferred from other diagnostics: accretion indicators (Muzerolle et al. 2000), as well as emission lines of simple atoms and molecules (Najita et al. 2010), including CO (e.g., Rettig et al. 2004). Based on a rotational diagram constructed from the infrared spectrum of CO fundamental ($v = 1-0$) rovibrational emission lines, Salyk et al. (2007) used a simple slab model to estimate $T = 650-1500$ K and $N_{\text{co}} = 0.2-1.4 \times 10^{19} \text{ cm}^{-2}$ for an emitting region that corresponds to $r \approx 0.1-1$ AU. Taking the mean temperature from the two CO lines, we find $T = 640-1660$ K and $N_{\text{co}} = 14-140 \times 10^{19} \text{ cm}^{-2}$ for our “hot” model in the same region – remarkably similar, keeping in mind that column density estimates from optically thick lines are inherently ambiguous. However, other analyses of the CO rovibrational spectrum suggest much lower temperatures (by a factor of ~ 2 ; Rettig et al. 2004; Pontoppidan et al. 2008; Salyk et al. 2009). Moreover, our “hot” model assumes enhanced temperatures over a continuous emitting area out to 4 AU: if a smaller area were adopted, the temperature scaling factor δT would have to be proportionately increased to compensate for the observed line wing intensities (notably to uncomfortable levels that start to impinge on the thermal dissociation energy). Given the uncertainties involved in analyzing both kinds of CO data, it is not clear whether a “hot” model derived from the rotational lines (as in §3.3.1) is necessarily in conflict

(i.e., too hot) with the rovibrational spectrum. In any case, it is interesting to note that these two complementary methods could eventually be used to obtain independent constraints on the gas properties inside the TW Hya dust disk cavity. In the near future, ALMA can provide sensitive high angular resolution images of these same CO transitions that will resolve the spatio-kinematic morphology of their line wings. That information will be crucial for locating the CO emitting area, enabling more direct comparisons between the infrared and millimeter-wave diagnostics.

While the first model described above was devoted to modifications of the *structure* in the inner disk, the remaining two alternatives focused on adjustments to the disk *kinematics*. Rather than increasing the intrinsic line intensities from a fixed emitting area, these other models produced the observed CO line wings by increasing the effective emitting area itself. In one such scenario, we modified the intrinsic velocity field in the inner disk with a simple parametric deviation from Keplerian orbits. We found in §3.3.2 that a model which incorporated super-Keplerian rotation in the inner disk successfully reproduced the observed CO line emission. Although there is considerable uncertainty involved, our “non-Keplerian” model rotated $\sim 30\%$ faster than Keplerian speeds at $r = 10$ AU, and $\sim 80\%$ faster at 1 AU ($f \approx 1.3$ and 1.8, respectively). If this deviation was restricted to much smaller disk radii only, the corresponding scaling factor f would need to be substantially larger to account for the observed CO line wings. Admittedly, of the three alternative models explored here, this scenario is the least physically-motivated. While in principle a (reverse) pressure gradient could accelerate the disk material, most models that consider such gradients instead call for sub-Keplerian motions (e.g., Weidenschilling 1977; Shu et al. 2007, 2008). However, it is possible that non-azimuthal gas velocities could mimic the parameterization used here. For example, a molecular outflow with high mass-loss rates, directed primarily in the vertical direction (a v_z component) and launched from the inner disk, might play a role. The TW Hya disk is thought to drive a substantial photoevaporative wind (e.g., Pascucci et al. 2011), but the molecular properties of that flow have not yet been explored in sufficient detail to easily compare with observations. Another example might be a velocity field with radial streaming motion (a v_r component), perhaps directed along spiral arms (e.g., Quillen et al. 2006). No such structural features have yet been identified for the TW Hya disk; but there are similar disks that do exhibit this kind of asymmetry (Weinberger et al. 1999; Augereau et al. 1999; Grady et al. 2001; Clampin et al. 2003; Fukagawa et al. 2004, 2006; Muto et al. 2012). Though these possibilities seem exotic, they remain in consideration until realistic, testable models for more complex disk velocity fields are developed.

The final alternative model we developed to account for the ALMA CO data also relied on modifying the *observed* disk velocity field, $v_{\text{obs}} = v_{\phi} \sin i$. In this scenario, we maintained the standard assumption of Keplerian orbits ($v_{\phi} = v_k$) and instead permitted the projection factor $\sin i$ to vary with radius. In §3.3.3, we developed a simple parametric description of a disk warp that simultaneously accounts for the CO line wings and the nearly face-on emission morphology near the systemic velocity. That simple model has an inclination of $\sim 4^\circ$ in the outer disk and increases only slightly to $\sim 10^\circ$ at $r = 1$ AU; the mean line-of-sight viewing angle averaged over the

disk area is comparable to the $\sim 4\text{--}7^\circ$ inferred previously (Krist et al. 2000; Weinberger et al. 2002; Qi et al. 2004; Hughes et al. 2011). Warps have been directly imaged in scattered light for the edge-on (effectively gas-free) debris disks around β Pic (Kalas & Jewitt 1995; Heap et al. 2000) and AU Mic (Liu 2004; Krist et al. 2005), and indirectly inferred from quasi-periodic photometric variations in optical/infrared light curves in other edge-on cases, notably KH 15D (Chiang & Murray-Clay 2004) and AA Tau (Bouvier et al. 1999). Warped viewing geometries have also been speculated for a few additional cases, including the disks around GM Aur (from CO spectral imaging; Dutrey et al. 1998; Hughes et al. 2009) and HD 100546 (from scattered light images; Quillen 2006).

In the specific case of the TW Hya disk, Roberge et al. (2005) have cited potential evidence for a warp based on an azimuthal asymmetry in their wideband *Hubble Space Telescope* (*HST*)/STIS coronagraphic images of optical light reflected off the disk surface. They identify a roughly sinusoidal variation of scattered light with the disk position angle in a region $\sim 1.3\text{--}1.6''$ from the central star, with a peak near P.A. = 234° and a trough near 54° (measured E of N, and notably roughly $\pm 90^\circ$ from the disk major axis orientation). Roberge et al. (2005) speculated that this azimuthal modulation in the brightness profile might be the consequence of a varying illumination pattern in the outer disk, generated by the shadowing effect of a warped disk geometry at much smaller radii. This is effectively the same type of model we have employed to explain the ALMA observations of the CO lines, so naturally we were motivated to test this possibility against the behavior of the Roberge et al. (2005) scattered light data. To do so, we implemented a simplified dust structure based on the “warp” model described in §3.3.3, assuming that the dust and gas are co-located outside a radius of 4 AU: to adhere to the dust modeling in the literature, we assume there is effectively no dust for $r < 4$ AU (e.g., Calvet et al. 2002; Hughes et al. 2007). We adopt the relative mass ratio, grain composition, and size distribution used in the disk atmosphere models of Andrews et al. (2012). The three-dimensional Monte Carlo radiative transfer code `RADMC-3D`⁴ (v0.30: C. P. Dullemond) was then used to generate a high-resolution synthetic image at a wavelength of $0.8\ \mu\text{m}$, assuming isotropic scattering. Following Roberge et al. (2005), we calculated a normalized intensity profile in 20° azimuthal bins in an annular ring from $r = 70\text{--}88$ AU.

The results are shown in Figure 6 and demonstrate a striking resemblance to the azimuthal modulation pattern inferred from the *HST*/STIS data (Roberge et al. 2005, see their Figure 9). Taken at face value, this remarkable agreement might be considered compelling independent evidence for a very modest warp in the TW Hya disk structure. Again, this scattered light model is *not* a fit to the *HST*/STIS observations of scattering off dust grains, but rather the predicted behavior based on one model that is able to describe ALMA observations of the CO gas structure. The sinusoidal pattern of the azimuthal profile is a result of material in the inner disk – where the warp is enhanced – shadowing dust at larger radii. The phase of that pattern is set by the assumed warp (rotation) axis, which was arbitrarily aligned with the observed major axis of the disk projected on the sky (151° E of N). However, in practice the phase depends only relatively weakly on

⁴[http://www.ita.uni-heidelberg.de/~sim\\$dullemond/software/radmc-3d/](http://www.ita.uni-heidelberg.de/~sim$dullemond/software/radmc-3d/)

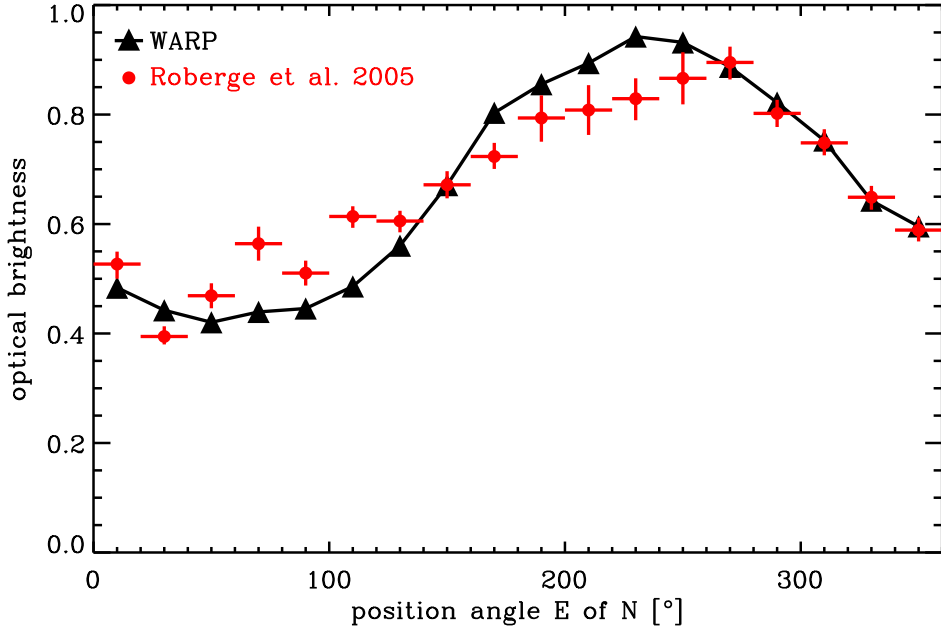


Fig. 6.— A comparison of the (normalized) azimuthal profile of optical light scattered off the TW Hya disk surface from both *HST*/STIS coronagraph data (*red circles*; Roberge et al. 2005) and a prediction based on our “warp” model (*black curve*; note that this is *not* a fit to the scattered light data). Both profiles were derived by averaging the intensities in 20° bins from an annulus extending from $r = 70$ -88 AU. The sinusoidal modulation is a natural consequence of shadowing by a warped structure in the inner disk (higher inclination angles at small radii), which produces a varying illumination pattern of the disk surface at larger radii.

the warp axis orientation: shifting the latter by $\pm 20^\circ$ leads to only modest changes to the pattern phase (i.e., the data are not quite able to quantify the warp orientation). The pattern amplitude depends more sensitively on the adopted model parameters, as it is set primarily by the height of the optically thick dust layer in the inner disk. If the inner disk were substantially cooler, and therefore had lower scale heights, the level of shadowing would decrease and the amplitude of the azimuthal scattering pattern would be diminished. Indeed, if we instead adopt the cooler, midplane dust temperatures found by (Andrews et al. 2012) to set the dust scale heights using Equation 4, we find a modest ($\sim 20\%$) decrease in the peak amplitudes that are more consistent with the scattered light data. Perhaps more important in this case is the truncation of the dust distribution for $r < 4$ AU. If we were to assume no dust depletion in the disk cavity, the shadowing of the outer disk would be much more pronounced, with a normalized amplitude of ~ 1 in the azimuthal variation of scattered light. In essence, there is a substantial degeneracy between the spatial distribution of dust in the inner disk (i.e., the cavity size and depletion factor, as well as the local scale heights) and the parameters that describe the warp. Nevertheless, for a set of simple assumptions grounded in the ALMA CO data (and the dust cavity from the SED and resolved images; Calvet et al. 2002;

Hughes et al. 2007; Andrews et al. 2012), we find a warp model is remarkably consistent with a key feature of the Roberge et al. (2005) scattered light data.

Warps have been postulated to originate from a wide range of phenomena, including gravitational instabilities (e.g., Sellwood 2010), intense radiation fields (Armitage & Pringle 1997), star-disk magnetic interactions (e.g., Terquem & Papaloizou 2000; Flaherty & Muzerolle 2010), and dynamical perturbations from a stellar flyby (Quillen 2006; Nixon & Pringle 2010). However, none of these seem particularly plausible in this case, given the known properties of TW Hya and its disk. In principle, a massive planet embedded in the inner disk with an orbit inclined out of the disk plane could also generate the modest warp inferred here (Lubow & Ogilvie 2001; Marzari & Nelson 2009). While this scenario has been extensively explored for the β Pic debris disk (Mouillet et al. 1997; Dawson et al. 2011), the high gas densities in the TW Hya disk could lead to the substantial damping of a planet inclination – and therefore the warp structure – on a relatively short (viscous) timescale (Papaloizou & Lin 1995). However, given the large uncertainties on the disk viscosities and densities, as well as the range of potential companion properties (e.g., masses, orbits), there is still a reasonable likelihood that a companion could maintain the modest orbital inclination required to sustain a small warp over the lifetime of the TW Hya disk (e.g., Bitsch & Kley 2011). Moreover, other effects related to planet-planet scattering in the system could produce repeated dynamical excitations of the gas disk (e.g., Thommes & Lissauer 2003).

We would be remiss not to point out that there is an alternative explanation for the Roberge et al. (2005) scattered light asymmetry: namely, a spatial variation in the scattering phase function of the grains. This latter possibility might better account for the observed kinks in the *radial* scattered light profiles, which incidentally our toy model does not reproduce well (although perhaps could, given a considerable modeling effort beyond the scope of this article). Other studies of the TW Hya scattered light disk from *HST* make no clear mention of an azimuthal asymmetry (e.g., Krist et al. 2000; Weinberger et al. 2002). The original WFPC2 discovery paper by Krist et al. (2000) does note that the “right” (we assume west) side of the disk appears brighter (consistent with the Roberge et al. asymmetry), but they suggest that the discrepancy could just as easily be explained by an instrumental or calibration artifact. We should also note that Pontoppidan et al. (2008) used infrared spectro-astrometry measurements of the CO fundamental rovibrational lines to determine an inclination of only $\sim 4\text{--}5^\circ$ in the inner $\sim 0.1\text{--}0.5$ AU of the TW Hya disk. The data presented here are not directly sensitive to such small radial scales, but the Pontoppidan et al. (2008) claim of a warped *outer* disk (where i is an increasing function of r) is clearly not consistent with the ALMA data. These inferred variations in inclination all could be compatible if the disk tilt is not monotonic with radius, but instead has some maximum inclination at a few AU. In any case, a simple warp model is a compelling potential explanation for both the ALMA CO spectral images and the *HST*/STIS scattered light data, but it is not necessarily the correct (or unique) solution.

In principle, all three of the alternative models that successfully explain the ALMA CO data could ultimately be produced by dynamical interactions between the disk and a companion located

a few AU from the central star. Nevertheless, despite the known dust depletion at small radii or potential evidence for a warp in this disk, there is not yet any firm evidence for a close companion to TW Hya. The most definitive high-resolution contrast limits for this system rule out companion masses $>0.014 M_{\odot}$ at 2-4 AU separations (Evans et al. 2012), suggesting that any perturber would need to be substellar or planetary in nature. A previous claim for a “hot Jupiter” (Setiawan et al. 2008) has been refuted (Huélamo et al. 2008; Rucinski et al. 2008), and, although there is a suggestive asymmetry in new mid-infrared data that is consistent with a faint point source near the edge of the disk cavity, its interpretation remains uncertain (Arnold et al. 2012). Along with deeper companion searches in the near future, we expect that some of the techniques presented here could be used to help provide new, empirical constraints on how dynamical interactions affect the kinematic and structural properties of the TW Hya gas disk and others like it.

5. Summary

We have studied the spatio-kinematic properties of the CO gas in the disk around the nearby young star TW Hya, making use of the ALMA science verification datasets provided during the facility construction. While these spectral images of the CO $J=2-1$ and $J=3-2$ emission lines from ALMA have only modest angular and spectral resolutions (and dynamic range), they provide roughly an order of magnitude improvement in sensitivity when compared to previous datasets (Qi et al. 2004, 2006; Hughes et al. 2011; Andrews et al. 2012). The key results of our analysis include:

1. We find clear evidence for substantial CO emission in high-velocity line wings, extending out to at least $\pm 2.1 \text{ km s}^{-1}$ from the systemic velocity. Assuming Keplerian rotation for a nearly face-on disk viewing geometry, the projected velocities of these wings correspond to intrinsic disk velocities $>20 \text{ km s}^{-1}$, indicating that they trace molecular gas at disk radii $\leq 2-5 \text{ AU}$.
2. Simple models that follow the standard prescription for analysing optically thick molecular lines are unable to simultaneously reproduce both the CO line wings and the spatially resolved emission morphology near the line cores. Instead, the ALMA data suggest that the inner regions of the TW Hya disk must have either much higher gas temperatures and/or a faster projected velocity field compared to what would be expected from emission in the outer disk.
3. Guided by those findings, we developed three alternative models that reproduce the ALMA data well by including small parametric modifications to the standard modeling prescription. One makes a substantial adjustment to the disk structure by scaling up the gas temperatures inside the known dust-depleted cavity in the TW Hya disk ($r < 4 \text{ AU}$). Two others include alterations to parameters describing the *observed* disk velocity field: the first by permitting the intrinsic velocities in the inner disk to increase to super-Keplerian rates, and the second by allowing the line-of-sight viewing angle of the disk to increase close to the central star.

The latter model of a disk warp finds some independent support in its ability to account for the azimuthal asymmetry noted in an optical scattered light image (Roberge et al. 2005).

4. Although no one model is explicitly favored by the current suite of ALMA data, they all include one implicit requirement: that there be a significant reservoir of molecular gas inside the ~ 4 AU-radius region in the TW Hya disk known to have diminished dust optical depths.

Perhaps most important, this study illustrates the impending capability of ALMA for providing a substantial advance in our understanding of molecular gas in protoplanetary disks. In principle, the powerful sensitivity of ALMA and the kind of kinematic super-resolution highlighted here will offer novel access to the characteristics of gaseous material in the innermost regions of these disks. In the near future, those capabilities will be supplemented with additional detail, as ALMA pushes toward significant improvements in both dynamic range and angular resolution as well.

We are grateful to Rebekah Dawson, Diego Muñoz, Christian Brinch, and Joanna Brown for their helpful suggestions, as well as the ALMA commissioning and science verification team for kindly providing detailed instructions that guided the calibration of these data. A.M.H. is supported by a fellowship from the Miller Institute for Basic Research in Science. The Atacama Large Millimeter/submillimeter Array (ALMA), an international astronomy facility, is a partnership of Europe, North America and East Asia in cooperation with the Republic of Chile. This article makes use of the following ALMA Science Verification data: ADS/JAO.ALMA#2011.0.00001.SV.

A. Notes on Three-Dimensional Rotations with Quaternions

In the general case, the rotation of a three-dimensional vector quantity can require some unwieldy algebraic manipulation. A much more elegant and straightforward technique to accomplish the same result relies on the use of the quaternion algebra developed by W. R. Hamilton in the 1840s.⁵ Although quaternions have been used in many aspects of physics (notably in the Dirac formulation of quantum mechanics) and are commonplace in fields like aerospace engineering and computer graphics, we have only rarely come across them in the astrophysics literature. If the warp structure postulated in §3.3.3 turns out to be a common disk feature, it might be useful to provide a brief tutorial on the use of quaternions in three-dimensional vector rotations.

Quaternions are a generalization of complex numbers. Any quaternion \mathbf{q} is represented by the combination of a scalar s and a vector $\vec{v} = (v_x, v_y, v_z)$, such that

$$\mathbf{q} = [s, \vec{v}] = [s, v_x, v_y, v_z]. \tag{A1}$$

⁵The original series of articles – entitled *On Quaternions, Or On a New System of Imaginaries in Algebra* and published in installments from 1844-1850 – is a recommended resource; it has been transcribed and edited by David R. Wilkins and graciously posted online: see <http://www.emis.ams.org/classics/Hamilton/OnQuat.pdf>.

Quaternion algebra has non-commutative multiplication

$$\mathbf{p} \star \mathbf{q} = [r, \vec{u}] \star [s, \vec{v}] = [r s - \vec{u} \cdot \vec{v}, r \vec{v} + s \vec{u} + \vec{u} \times \vec{v}], \quad (\text{A2})$$

an inner product, $\mathbf{p} \cdot \mathbf{q} = [r, \vec{u}] \cdot [s, \vec{v}] = r s + \vec{u} \cdot \vec{v}$, and conjugation, $\bar{\mathbf{q}} = [s, -\vec{v}] = [s, -v_x, -v_y, -v_z]$. For the specific task of applying a rotation, the definitions of an angle θ and a rotation axis \vec{a} can be compactly encoded in a quaternion, where

$$\mathbf{q} = [\cos(\theta/2), \vec{a} \sin(\theta/2)]. \quad (\text{A3})$$

Any vector \vec{v} can be properly mapped into its rotated counterpart \vec{w} by generating corresponding quaternions with zero scalar components, $\mathbf{v}_0 = [0, \vec{v}]$ and $\mathbf{w}_0 = [0, \vec{w}]$, and then applying a simple quaternion algebra manipulation,

$$\mathbf{w}_0 = \mathbf{q} \star \mathbf{v}_0 \star \bar{\mathbf{q}}. \quad (\text{A4})$$

A Worked Example: To demonstrate more concretely how the formalism described above can be used in practice, we describe the methodology used in §3.3.3 to apply a warp rotation to the model disk described in §3.1. For simplicity, we assume that the rotation axis corresponds with the Cartesian x -axis, so that $\vec{a} = (1, 0, 0)$ by definition. In our models, this axis is by default aligned with the observed major axis position angle, oriented 151° E of N projected on the sky. We considered a rotation by an angle $i(r)$, which depended on the distance from the model center, $r = \sqrt{x^2 + y^2}$ (see §3.3.3; Equation 8). In that context, consider a parcel of gas located at $\vec{v} = (x_p, y_p, z_p)$ where $x_p = z_p = 0$ and $y_p = 1$ AU (i.e., 1 AU along the y -axis, perpendicular to the warp rotation axis, and in the disk midplane). The quaternion $\mathbf{v}_0 = [0, \vec{v}]$ describes the parcel position. Likewise, the warp – a radially varying rotation – is also encoded in a quaternion, $\mathbf{q} = [\cos(i/2), \sin(i/2), 0, 0]$.

The warp can be applied following Equation A4, and will result in a rotated position for the initial gas parcel that corresponds to the vector component of the quaternion

$$\begin{aligned} \mathbf{w}_0 &= [\cos(i/2), \sin(i/2), 0, 0] \star [0, 0, y_p, 0] \star [\cos(i/2), -\sin(i/2), 0, 0] \\ &= [0, 0, y_p(\cos^2(i/2) - \sin^2(i/2)), 2y_p \cos(i/2) \sin(i/2)] \\ &= [0, 0, y_p \cos i, y_p \sin i], \end{aligned} \quad (\text{A5})$$

where the final step employed elementary trigonometric identities to recover the simple result expected for a cell originally located orthogonal to the rotation axis. Using the parameters in Table 2 to reconstruct the angle i , the updated location of the gas parcel after rotation is described by $\mathbf{w}_0 = [0, 0, 0.98 \text{ AU}, 0.18 \text{ AU}]$; that is, slightly closer to the rotation axis and now lying at some modest height ($z = 0.18 \text{ AU}$) above the midplane. Repeating this approach for all model locations initially in the midplane ($z_p = 0$) produces the warped structure sketched in Figure 7.

Of course, the algebra involved in reproducing Equation A5 is substantially more complex for a more general location \vec{v} , validating the simplicity in the quaternion approach encapsulated in Equa-

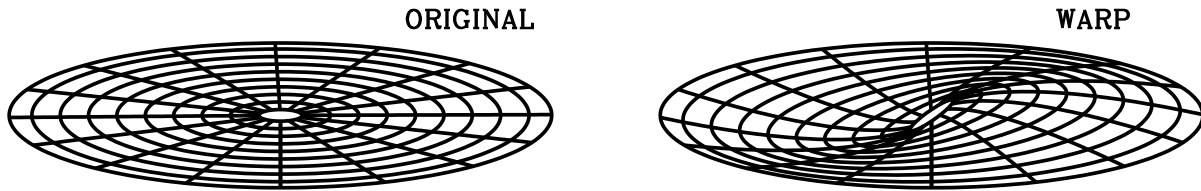


Fig. 7.— Schematic of a flat model grid (*left*) in the disk plane ($z = 0$) and its warped counterpart after a quaternion rotation (*right*). Given the modest rotation postulated in §3.3.3, the grids are shown with an extreme aspect ratio of 1:1:20 to highlight the subtle warp about the x -axis.

tion A4. For interested users, there are established and well-documented quaternion manipulation packages available online for both IDL⁶ and `python`⁷ (among other common coding packages).

⁶<http://cow.physics.wisc.edu/~simscraig/idl/math.html>

⁷[http://cxc.harvard.edu/mta/ASPECT/tool\\$_-doc/pydocs/Quaternion.html](http://cxc.harvard.edu/mta/ASPECT/tool$_-doc/pydocs/Quaternion.html)

Table 1. Synthesized Channel Map Properties

line	Δv [km s ⁻¹]	noise (1σ) [Jy beam ⁻¹]	peak I_ν [Jy beam ⁻¹]	F_ν [Jy km s ⁻¹]
¹² CO $J=2-1$	0.20	0.009	7.8 ± 0.8	17.5 ± 1.8
	0.35	0.008	7.3 ± 0.7	17.5 ± 1.8
¹² CO $J=3-2$	0.12	0.020	9.7 ± 1.0	37.2 ± 3.7
	0.35	0.015	10.6 ± 1.1	36.0 ± 3.6

Note. — Properties of the synthesized channel maps at native and binned spectral resolutions. The noise is defined as the RMS variation per *channel* in line-free regions. The peak I_ν refers to the peak intensity in a channel of fixed width Δv . The integrated flux densities ($F_\nu = \int I_\nu dv$) correspond to the sum of the emission at all velocities in a $5'' \times 5''$ square box centered on the stellar position. The quoted errors include a $\sim 10\%$ systematic uncertainty in the absolute flux scale.

Table 2. Model Parameters

parameter	units	fiducial	high- q	high- M_*	high- i	hot	non-Kep	warp
$\log N_{10}$	[cm^{-2}]	19.00	19.42	19.28	19.60	19.00	18.81	18.83
γ	...	0.99	0.99	0.66	0.90	0.99	0.94	0.93
r_c	[AU]	28	28	36	24	28	32	33
T_{10} (2–1)	[K]	77	110	75	68	77	100	100
(3–2)	[K]	88	115	94	90	88	99	104
q (2–1)	...	0.38	0.65	0.39	0.32	0.38	0.49	0.53
(3–2)	...	0.44	0.65	0.51	0.49	0.44	0.49	0.53
ξ	[m s^{-1}]	20	20	10	10	20	20	15
M_*	[M_\odot]	0.8	0.8	1.5	0.8	0.8	0.8	0.8
i_{10}	[$^\circ$]	5.8	5.8	6.0	8.0	5.8	5.7	7.5
y	...	0	0	0	0	0	0	0.15
r_b	[AU]	57	...
x	...	0	0	0	0	0	0.15	0
δT	...	1	1	1	1	3	1	1

Note. — The parameter values adopted in the modeling analysis in §3.2 and 3.3. Each column corresponds to a different model type, and each row represents a different model parameter (the subscript ‘10’ denotes that parameter value at $r = 10$ AU). Note that only the “warp” model has a spatially varying disk inclination: in all other cases $i_{10} = i$ at all radii, and $y = 0$ by definition (see §3.3.3). The parameter r_b is only defined for the “non-Keplerian” model; in all other cases $x = 0$ (or $f = 1$, at all radii; see §3.3.2). The parameter δT corresponds to a constant scaling of the temperature profile for $r < 4$ AU in the “hot” model only: all other models have $\delta T = 1$ by definition.

REFERENCES

- Andrews, S. M., Wilner, D. J., Hughes, A. M., Qi, C., & Dullemond, C. P. 2009, *ApJ*, 700, 1502
- Andrews, S. M., Wilner, D. J., Hughes, A. M., Qi, C., & Dullemond, C. P. 2010, *ApJ*, 723, 1241
- Andrews, S. M., et al. 2012, *ApJ*, 744, 162
- Armitage, P. J., & Pringle, J. E. 1997, *ApJ*, 88, L47
- Arnold, T. J., Eisner, J. A., Monnier, J. D., & Tuthill, P. 2012, *ApJ*, 750, 119
- Augereau, J. C., Lagrange, A. M., Mouillet, D., & Ménard, F. 1999, *A&A*, 350, L51
- Beckwith, S. V. W., & Sargent, A. I. 1993, *ApJ*, 402, 280
- Bitsch, B., & Kley, W. 2011, *A&A*, 530, A41
- Bouvier, J., et al. 1999, *A&A*, 349, 619
- Brinch, C., & Hogerheijde, M. R. 2010, *A&A*, 523, A25
- Calvet, N., D’Alessio, P., Hartmann, L., Wilner, D. J., Walsh, A., & Sitko, M. 2002, *ApJ*, 568, 1008
- Cassen, P., & Moosman, A. 1981, *Icarus*, 48, 353
- Chiang, E. I., & Murray-Clay, R. A. 2004, *ApJ*, 607, 913
- Clampin, M., et al. 2003, *AJ*, 126, 385
- Corder, S., Eisner, J., & Sargent, A. 2005, *ApJ*, 622, L133
- Dawson, R. I., Murray-Clay, R. A., & Fabrycky, D. C. 2011, *ApJ*, 743, L17
- Dutrey, A., Guilloteau, S., & Simon, M. 1994, *A&A*, 286, 149
- Dutrey, A., Guilloteau, S., Prato, L., Simon, M., Duvert, G., Schuster, K., & Ménard, F. 1998, *A&A*, 338, L63
- Dutrey, A., et al. 2008, *A&A*, 490, L15
- Evans, T. M., Ireland, M. J., Kraus, A. L., et al. 2012, *ApJ*, 744, 120
- Flaherty, K. M., & Muzerolle, J. 2010, *ApJ*, 719, 1733
- Fukagawa, M., et al. 2004, *ApJ*, 605, L53
- Fukagawa, M., et al. 2006, *ApJ*, 636, L153

- Grady, C. A., et al. 2001, *AJ*, 122, 3396
- Guilloteau, S., & Dutrey, A. 1998, *A&A*, 339, 467
- Hartmann, L., Calvet, N., Gullbring, E., & D’Alessio, P. 1998, *ApJ*, 495, 385
- Heap, S. R., Lindler, D. J., Lanz, T. M., Cornett, R. H., Hubeny, I., Maran, S. P., & Woodgate, B. 2000, *ApJ*, 539, 435
- Huélamo, N., et al. 2008, *A&A*, 489, L9
- Hughes, A. M., Wilner, D. J., Calvet, N., D’Alessio, P., Claussen, M. J., & Hogerheijde, M. R. 2007, *ApJ*, 664, 536
- Hughes, A. M., Wilner, D. J., Qi, C., & Hogerheijde, M. R. 2008, *ApJ*, 678, 1119
- Hughes, A. M., et al. 2009, *ApJ*, 698, 131
- Hughes, A. M., Wilner, D. J., Andrews, S. M., Qi, C., & Hogerheijde, M. R. 2011, *ApJ*, 727, 85
- Kalas, P., & Jewitt, D. 1995, *AJ*, 110, 794
- Koerner, D. W., Sargent, A. I., & Beckwith, S. V. W. 1993, *Icarus*, 106, 2
- Koerner, D. W., & Sargent, A. I. 1995, *AJ*, 109, 2138
- Krist, J. E., Stapelfeldt, K. R., Ménard, F., Padgett, D. L., & Burrows, C. J. 2000, *ApJ*, 538, 793
- Krist, J. E., et al. 2005, *AJ*, 129, 1008
- Lin, S.-Y., Ohashi, N., Lim, J., Ho, P. T. P., Fukagawa, M., & Tamura, M. 2006, *ApJ*, 645, 1297
- Liu, M. C. 2004, *Science*, 305, 1442
- Lubow, S. H., & Ogilvie, G. I. 2001, *ApJ*, 560, 997
- Lynden-Bell, D., & Pringle, J. E. 1974, *MNRAS*, 168, 603
- Mannings, V., & Sargent, A. I. 1997, *ApJ*, 490, 792
- Markwardt, C. B. 2009, in *Astronomical Society of the Pacific Conference Series*, Vol. 411, *Astronomical Data Analysis Software and Systems XVIII*, ed. D. A. Bohlender, D. Durand, & P. Dowler, 251
- Marzari, F., & Nelson, A. F. 2009, *ApJ*, 705, 1575
- Mouillet, D., Larwood, J. D., Papaloizou, J. C. B., & Lagrange, A. M. 1997, *MNRAS*, 292, 896
- Muto, T., et al. 2012, *ApJ*, 748, L22

- Muzerolle, J., Calvet, N., Briceño, C., Hartmann, L.,
Najita, J. R., et al. 2010, *ApJ*, 712, 274
- Nixon, C. J., & Pringle, J. E. 2010, *MNRAS*, 403, 1887
- Papaloizou, J. C. B., & Lin, D. N. C. 1995, *ApJ*, 438, 841
- Pascucci, I., et al. 2011, *ApJ*, 736, 13
- Piétu, V., Guilloteau, S., & Dutrey, A. 2005, *ApJ*, 443, 945
- Pontoppidan, K. M., Blake, G. A., van Dishoeck, E. F., Smette, A., Ireland, M. J., & Brown, J. 2008, *ApJ*, 684, 1323
- Qi, C., et al. 2004, *ApJ*, 616, L11
- Qi, C., et al. 2006, *ApJ*, 636, L157
- Quillen, A. C. 2006, *ApJ*, 640, 1078
- Quillen, A. C., Varnière, P., Minchev, I., & Frank, A. 2006, *AJ*, 129, 2481
- Rettig, T. W., Haywood, J., Simon, T., Brittain, S. D., & Gibb, E. 2004, *ApJ*, 616, L163
- Roberge, A., Weinberger, A. J., & Malumuth, E. M. 2005, *ApJ*, 622, 1171
- Rucinski, S. M., et al. 2008, *MNRAS*, 391, 1913
- Salyk, C., Blake, G. A., Boogert, A. C. A., & Brown, J. M. 2007, *ApJ*, 655, L105
- Salyk, C., Blake, G. A., Boogert, A. C. A., & Brown, J. M. 2009, *ApJ*, 699, 330
- Schöier, F. L., van der Tak, F. F. S., van Dishoeck, E. F., & Black, J. H. 2005, *A&A*, 432, 369
- Sellwood, J. A. 2010, in *Planets, Stars, & Stellar Systems Vol. 5*, ed. G. Gilmore (arXiv:1006.4855)
- Setiawan, J., Henning, T., Launhardt, R., Müller, A., Weise, P., & Kürster, M. 2008, *Nature*, 451, 38
- Shu, F. H., Galli, D., Lizano, S., Glassgold, A. E., & Diamond, P. H. 2007, *ApJ*, 665, 535
- Shu, F. H., Lizano, S., Galli, D., Cai, M. J., & Mohanty, S. 2008, *ApJ*, 682, L121
- Simon, M., Dutrey, A., & Guilloteau, S. 2000, *ApJ*, 545, 1034
- Terebey, S., Shu, F. H., & Cassen, P. 1984, *ApJ*, 286, 529
- Terquem, C., & Papaloizou, J. C. B. 2000, *A&A*, 360, 1031

Thommes, E. W., & Lissauer, J. J. 2003, *ApJ*, 597, 566

van Leeuwen, F. 2007, *A&A*, 474, 653

Weidenschilling, S. J. 1977, *MNRAS*, 180, 57

Weinberger, A. J., et al. 1999, *ApJ*, 535, L53

Weinberger, A. J., et al. 2002, *ApJ*, 566, 409

Wichmann, R., Bastian, U., Krautler, J., Jankovics, I., & Rucinski, S. M. 1998, *MNRAS*, 301, L39